NANO LETTERS

Piezostrain-Driven Bidirectional Enhancement of Optical Synaptic Plasticity in Wafer-Scale Co-Phased Tin Selenide Layers

Changhyeon Yoo, Sang Sub Han, Chung Won Lee, Jebadiah Pond, Yu-Jin Song, Jung Han Kim, and Yeonwoong Jung*

Cite This: *Nano Lett.* 2025, 25, 106−114 Read Online

ACCESS | Metrics & More | Article Recommendations | Supporting Information

ABSTRACT: Tin (Sn)-based two-dimensional (2D) materials exhibit intriguing mechanical and optoelectrical properties owing to their non-centrosymmetric crystallinity and tunable band structures. A judicious integration of these individually decoupled properties is projected to introduce unparalleled functionalities into them, which remain largely unexplored. Herein, we develop wafer-scale tin selenide ($SnSe_{2-x}$, $0 < x < 1$) 2D layers composed of thermodynamically stable coexisting phases of SnSe and $SnSe_2$ with distinct functionalities and identify a strong interplay between their mechanical and optoelectrical characteristics. Mechanically, they display a strain-dependent piezoelectricity upon an anisotropic deformation of convex vs concave bending. Optoelectrically, they present an optical pulse-induced potentiation and synaptic plasticity accompanying a wavelength-tunable photoconduction upon visible to near-infrared (IR) illuminations. Harnessing these two independent features in a coupled manner enables a drastic enhancement of their synaptic responsiveness by >40% with a piezostrain of <1%. These findings suggest opportunities for atomically thin semiconductors in mechano-optical neuromorphic device applications.

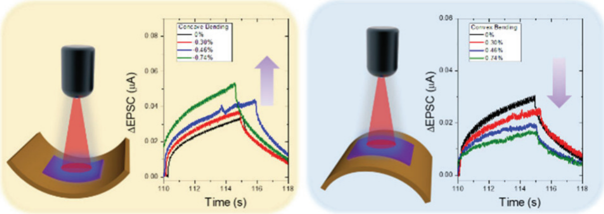

KEYWORDS: *Tin Selenide, 2D $SnSe_{2-x}$, Artificial Synapse, Neuromorphic Application, Synaptic Plasticity, Piezo-phototronics*

Developing next-generation optoelectronics and neuromorphic applications demands advanced photoresponsive materials with unconventional structures and multifunctionalities as device building blocks. In this regard, atomically thin 2D $SnSe_{2-x}$ layers of controlled chemistries (i.e., $0 < x < 1$) have drawn significant attention due to their extraordinary optoelectronic and piezoelectric characteristics.[1−4] They are thermodynamically stable in two distinct structural phases and compositional stoichiometries of tin monoselenide (SnSe) and tin diselenide ($SnSe_2$). SnSe exhibits excellent thermoelectric and piezoelectric properties owing to its non-centrosymmetric nature, enabling mechanical stress-driven polarizations.[3,5] This p-type semiconductor with a bandgap of ~1.0 eV accordingly presents deformation-driven anisotropic electrical and optical properties useful for various applications.[2,6−8] Conversely, $SnSe_2$ is an n-type semiconductor with a similar bandgap but possesses a hexagonal CdI_2-type crystal structure. It stands out for its strong photoresponsiveness in a broadband spectral range of visible to near-IR; thus, it is particularly promising for optoelectronic devices.[2,8−10] Recent studies have attempted to explore 2D $SnSe_{2-x}$ layers composed of co-phased SnSe and $SnSe_2$, aiming to realize their unconventional yet superior functionalities.[5,11−13] Synergistically modulating the distinct functionalities of each constituent SnSe and $SnSe_2$ with various external stimuli such as mechanical strains and optical pulses can dynamically harness device performances.[14−16] For example, this "coupling" approach enables a precise tuning of photoresponsiveness under controlled deformation conditions,[14,17] which projects expanded opportunities toward emerging technologies such as artificial synapses and neuromorphic systems.[18−20]

Herein, we report on a significant enhancement of optically modulated synaptic plasticity in wafer-scale (>cm^2) flexible 2D $SnSe_{2-x}$ layers containing two phases of SnSe and $SnSe_2$ via bidirectionally applied piezostrains. The 2D layers are grown via a low-temperature chemical vapor deposition (CVD) process in a range of 150 to 300 °C, accompanying a temperature-dependent phase transition of SnSe to $SnSe_2$. They exhibit deformation orientation-dependent piezoelectricity and wavelength-tunable broadband-responsiveness, simultaneously leveraging characteristics of SnSe and $SnSe_2$, respectively. Such independently realized piezo- and optical properties are synergistically coupled to demonstrate an

Received: September 5, 2024
Revised: December 7, 2024
Accepted: December 13, 2024
Published: December 18, 2024

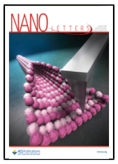

https://doi.org/10.1021/acs.nanolett.4c04371

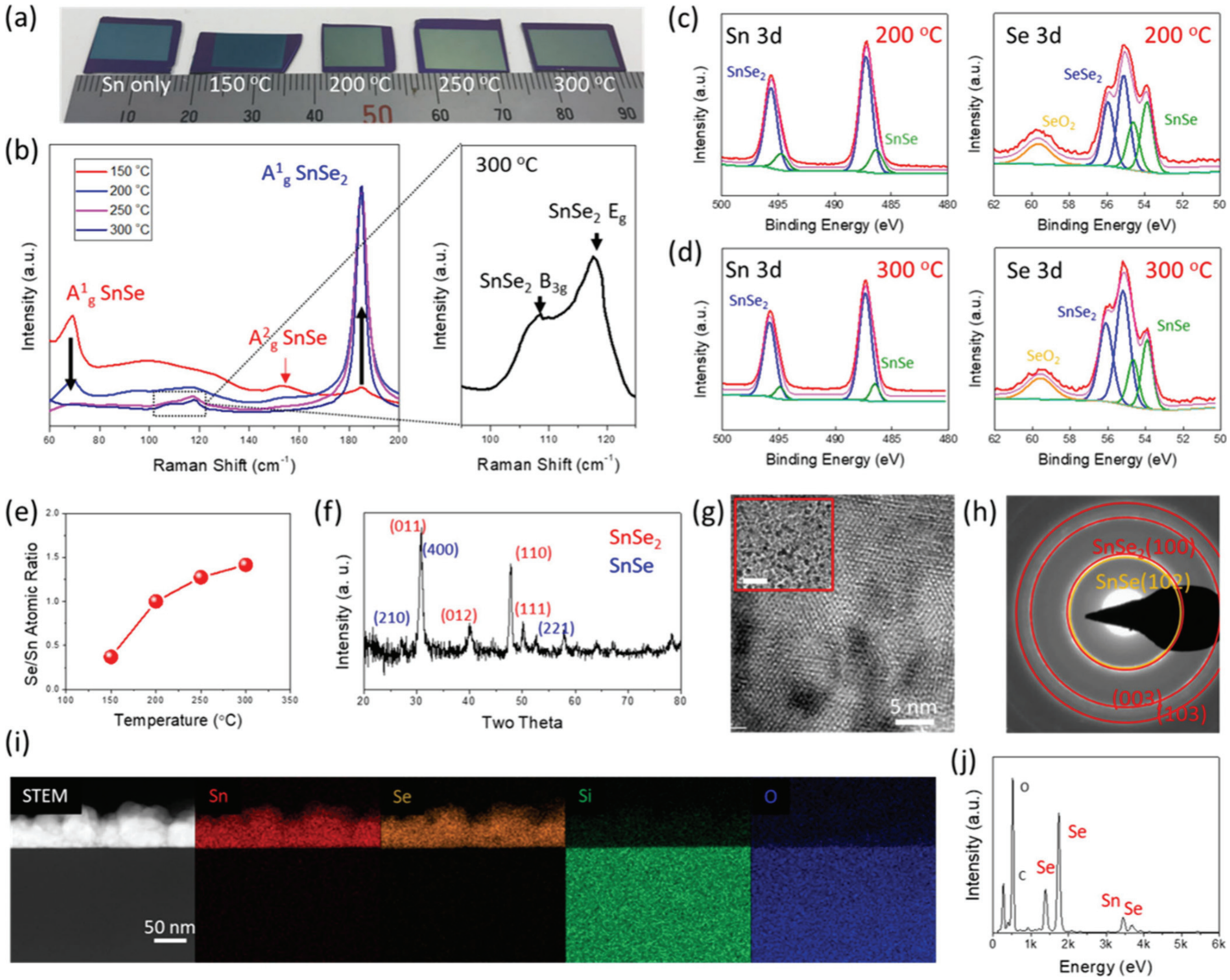

Figure 1. Characterization of low-temperature CVD-grown centimeter-scale 2D $SnSe_{2-x}$ layers: (a) Images of 2D $SnSe_{2-x}$ layers grown on SiO_2/Si wafers prepared at various CVD temperature. (b) Raman spectra of 2D $SnSe_{2-x}$ layers grown at various CVD temperature. (c, d) High-resolution core-level XPS spectra of Sn 3d (left) and Se 3d (right) obtained from 2D $SnSe_{2-x}$ layers grown at (c) 200 °C and (d) 300 °C. (e) Growth temperature-dependent atomic ratio of Se/Sn. (f) XRD patterns of 2D $SnSe_{2-x}$ layers grown at 300 °C. (g) Plane-view HR-STEM image and its corresponding low-magnification image (inset). (h) SAED pattern corresponding to (g) confirming a coexistence of SnSe and $SnSe_2$ phases. (i) Cross-sectional EDS elemental mapping images of 2D $SnSe_{2-x}$ layers. (j) EDS spectrum corresponding to (i).

optically potentiated artificial synaptic plasticity and its piezostrain-driven enhancements.

Figure 1a shows an image of wafer-scale 2D $SnSe_{2-x}$ layers prepared with an identical Sn thickness of 24 nm at various CVD temperatures, with growth conditions detailed in the Experimental Methods section of the Supporting Information. Despite the constant thickness of Sn seed films, a noticeable progression of color changes is observed with increasing temperature, suggesting variations in the thicknesses and chemical compositions of the resulting samples. In fact, atomic force microscopy (AFM) characterizations (Supporting Information Figure S1) reveal a systematic increase of the thickness with increasing temperature, indicating a temperature-dependent transition of structural phases across the samples, to be clarified in the next section. Raman spectroscopy characterizations were performed to identify the chemical structures of the samples, as presented in Figure 1b. For the samples grown at lower temperatures (e.g., 150 °C), two distinct peaks at 69.35 and 153.45 cm^{-1} are observed, corresponding to the A^1_g and A^2_g vibration modes of SnSe.[3,21] Interestingly, these peaks are gradually suppressed with reduced intensities as the CVD temperature increases. Furthermore, additional peaks appear at multiple locations, e.g., dominantly at 185.27 cm^{-1}, which becomes more pronounced with increasing temperatures. For example, an enlarged view of the Raman spectrum for the sample grown at 300 °C shows small peaks at 108.64 and 118.26 cm^{-1}, along with a strong peak at 185.27 cm^{-1}, corresponding to the B_{3g}, E_g, and A^1_g vibration modes of $SnSe_2$, respectively.[21,22] This observation indicates a temperature-dependent transition of SnSe to $SnSe_2$, suggesting a coexistence of SnSe and $SnSe_2$ in the samples, both of which are known to be thermodynamically stable depending on temperatures.[21,22] The oxidation states of the $SnSe_{2-x}$ samples prepared at four different temperatures were inspected by using X-ray photoelectron spectroscopy (XPS). XPS spectra of Sn 3d and Se 3d core-level binding energies are presented for two representative samples grown at 200 °C (Figure 1c) and 300 °C (Figure 1d). In

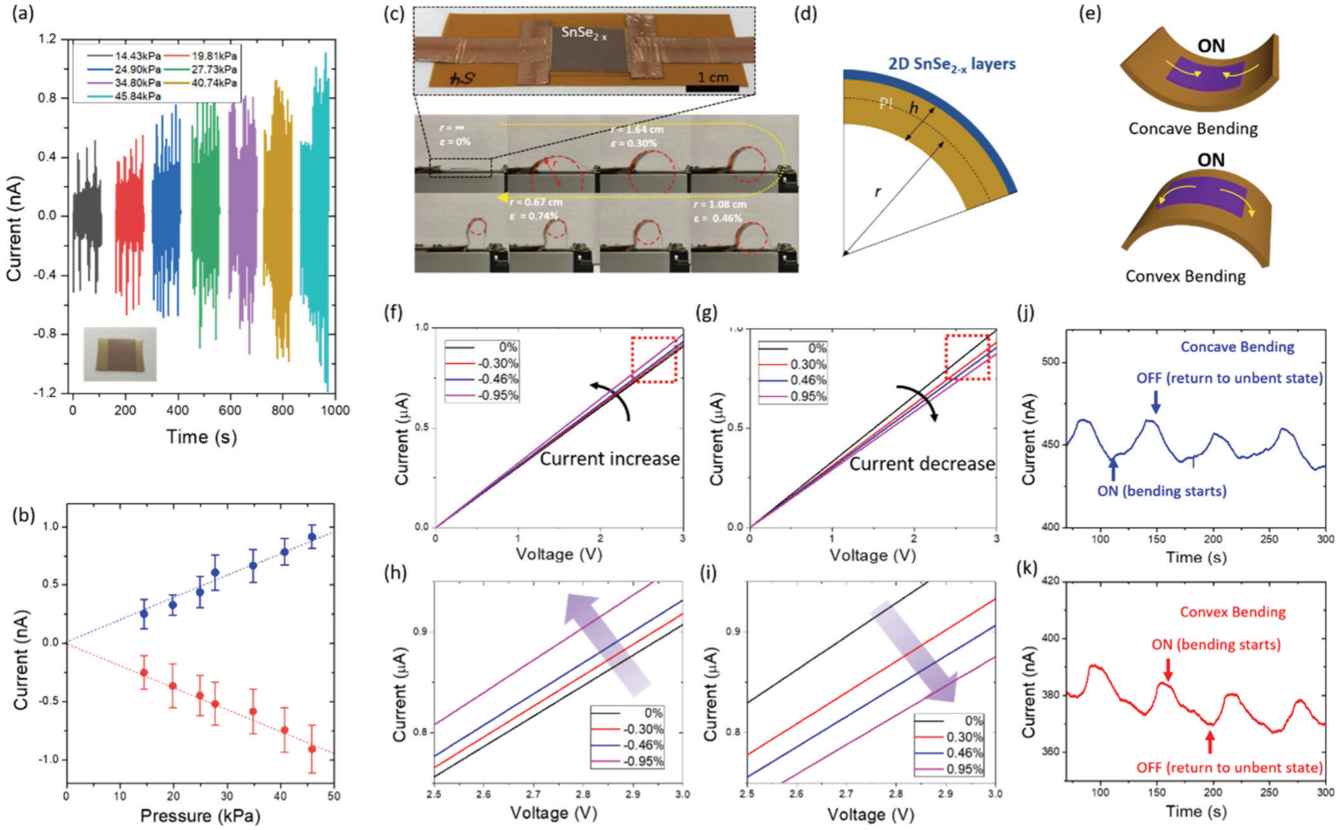

Figure 2. Confirmation of intrinsic piezoelectricity in $SnSe_{2-x}$/PI and its anisotropic deformation-driven piezo-current generation: (a) Temporal response plots of piezo-current generation with increasing pressure values along with its corresponding sample image (inset). (b) Correlation of applied pressure and generated current during compression (blue) and release (red) cycles. (c) Images of the $SnSe_{2-x}$/PI sample (top) and its sequential bending (bottom). (d) Diagram to calculate bending strain values. (e) Schematic illustrations of concave and convex bending applied to $SnSe_{2-x}$/PI. (f, g) $I-V$ characteristics obtained under varying strain conditions: (f) concave (compressive) bending and (g) convex (tensile) bending. (h, i) Enlarged views of the red boxes in (f) and (g), corresponding to (f) concave and (g) convex bending, respectively. (j, k) Temporal responses of current changes obtained during cycles of (j) concave and (k) convex bending, respectively.

Figure 1c, the XPS spectra of the sample grown at 200 °C reveal two distinct Sn 3d doublets, with the first at 486.4 and 494.8 eV corresponding to the Sn^{2+} states of SnSe, and the second at 487.3 and 495.7 eV indicating the Sn^{4+} states of $SnSe_2$.[5,21,23,24] Similarly, the Se 3d spectra show doublets at 53.7 and 54.6 eV for SnSe and the others at 55.1 and 55.8 eV for $SnSe_2$.[5,21,23,24] The sample grown at 300 °C also displays two doublets, as presented in Figure 1d. The Sn 3d peaks at 486.5 and 494.9 eV are associated with Sn^{2+} of SnSe, while the peaks at 487.4 and 495.7 eV correspond to Sn^{4+} of $SnSe_2$. The Se 3d spectra show similar patterns with doublets at 53.9 and 54.7 eV for SnSe and at 55.2 and 56.0 eV for $SnSe_2$.[5,21,23,24] These findings confirm that the $SnSe_{2-x}$ samples are composed of a mixture of stoichiometric $SnSe_2$ and SnSe phases, whose XPS peak positions are all consistent with previous studies.[5,21,23,24] The chemical compositions (i.e., x values) of the $SnSe_{2-x}$ samples are quantified by XPS analysis, yielding temperature-variant atomic ratios: Sn:Se = 73:27 (150 °C), 50:50 (200 °C), 44:56 (250 °C), and 41:58 (300 °C). All the corresponding XPS spectra are presented in the Supporting Information, Figure S2. A correlation of Sn:Se ratios vs CVD temperature is provided in Figure 1e, which confirms a transition of SnSe to $SnSe_2$, i.e., toward Se-rich phases with increasing temperatures. It is worth mentioning that these comprehensive observations of the temperature-dependent phase transition well agree with the temperature-dependent thickness increase of $SnSe_{2-x}$ samples (Supporting Information, Figure S1), reflecting a gradual temperature-dependent increase of Se concentration. Among the compositionally variant samples prepared at four different temperatures, we chose to employ the 300 °C samples for further structural characterizations and optoelectronic applications based on the following justifications: (1) Samples grown at higher temperatures exhibit better optoelectronic performances due to an abundance of more photoresponsive $SnSe_2$ over SnSe. (2) Simultaneously, the CVD growth temperature should not be too high, as polymers such as polyimide (PI) will be employed as growth substrates for demonstrations of flexible optoelectronics. The demonstrated CVD process allows for the direct growth of $SnSe_{2-x}$ films on PI substrates without requiring additional postdeposition chemical treatments or complex multistep procedures, ensuring scalability and practicality for large-scale device applications. Figure 1f presents an X-ray diffraction (XRD) pattern obtained from a sample grown at 300 °C, revealing a coexistence of crystalline SnSe and $SnSe_2$ phases. The SnSe XRD peaks observed at 27.02°, 30.99°, and 52.74° correspond to the orthorhombic SnSe structure (i.e., *Pnma* (62) space group) with lattice planes of (210), (400), and (221), respectively, according to ICDD No. 32-1382.[25,26] Also, the $SnSe_2$ XRD peaks at 30.90°, 39.90°, 47.82°, and 50.14° correspond to the hexagonal $SnSe_2$ structure (i.e., $P\bar{3}m1$ (164) space group) with lattice planes of (011), (012), (110),

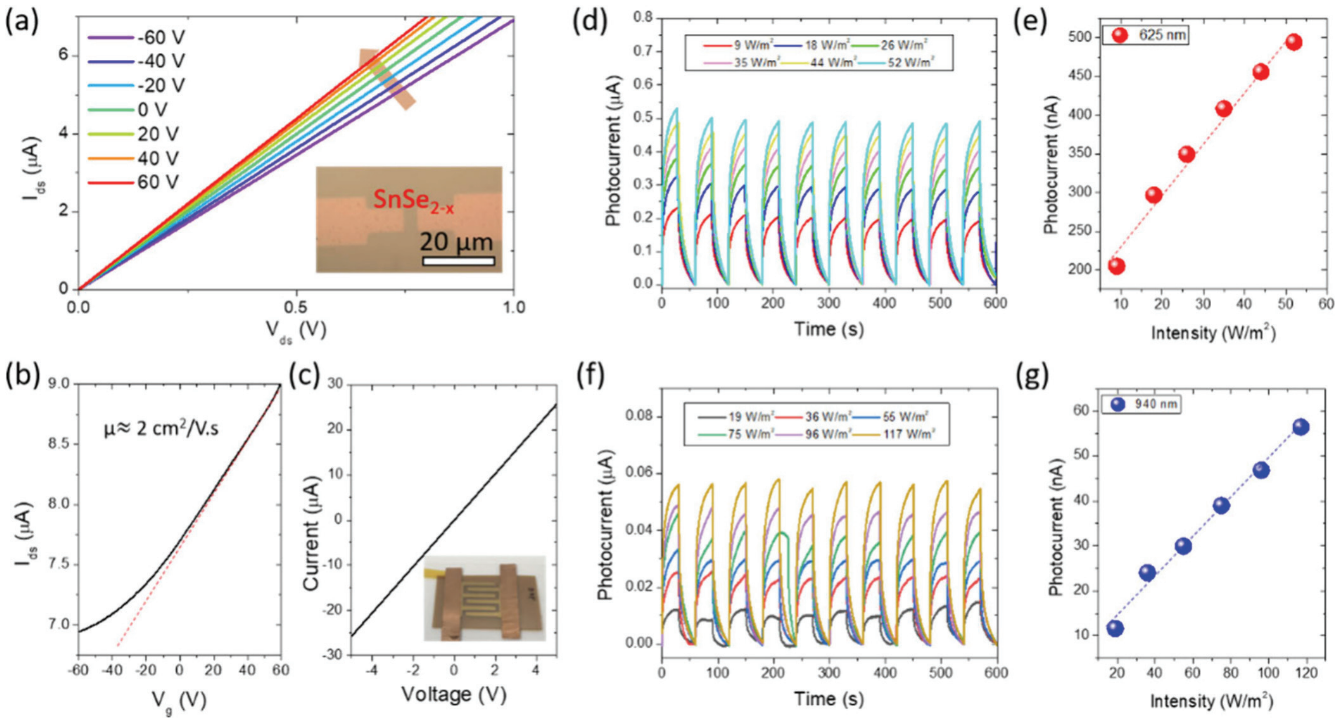

Figure 3. Confirmation of semiconducting nature and broadband (i.e., visible to near-IR) photoresponsiveness of 2D $SnSe_{2-x}$ layers. (a) FET I_{ds}−V_{ds} transfer characteristics of 2D $SnSe_{2-x}$ layers indicating an n-type semiconducting transport along with the corresponding sample image (inset). (b) I_{ds}−V_g transfer curve revealing an electron mobility (μ) of ∼2 cm^2 V^{-1} s^{-1}. (c) Ohmic transport of $SnSe_{2-x}$/PI with IDE-patterned Au electrodes and its corresponding sample image (inset). (d) Time-dependent photocurrents of $SnSe_{2-x}$/PI under periodic 625 nm illumination with varying intensities. (e) Intensity-dependent linear generation of photocurrent at 625 nm. (f) Time-dependent photocurrents under periodic 940 nm illumination with varying intensities. (g) Intensity-dependent linear generation of photocurrent at 940 nm.

and (111), respectively, according to ICDD 01-089-2939.[27,28] Figure 1g presents a high-resolution (HR) transmission electron microscopy (TEM) image of the 300 °C $SnSe_{2-x}$ sample, revealing the polycrystalline structure of CVD-grown 2D van der Waals (vdW) layered crystals.[29−31] The inset shows the corresponding plane-view low-magnification TEM image. A cross-sectional HR-TEM image of another sample is presented in the Supporting Information, Figure S3, which shows a mixed orientation of vertically slanted 2D vdW layers. Figure 1h displays a selected area electron diffraction (SAED) pattern of the 2D $SnSe_{2-x}$ layers, which is indexed by the (102) plane (orange) of SnSe along with the (100), (003), and (103) ring patterns (red) of $SnSe_2$. Observations of these indexed ring patterns indicate that the 2D $SnSe_{2-x}$ layers are in a polycrystalline structure composed of both SnSe and $SnSe_2$ phases, consistent with XRD characterizations. Figure 1i shows cross-sectional energy dispersive X-ray spectroscopy (EDS) elemental mapping images of the 2D $SnSe_{2-x}$ layers grown on a SiO_2/Si wafer in scanning TEM (STEM) mode. The images visualize a compositional uniformity of constituent Sn and Se, indicating a spatial homogeneity of the co-phased SnSe and $SnSe_2$. The corresponding EDS atomic fraction line profiles are presented in the Supporting Information, Figure S4. Figure 1j displays a representative EDS spectrum where x is in a typical range of ∼0.15 to 0.5, varying with sample preparation conditions.

The intrinsic piezoelectricity of the 2D $SnSe_{2-x}$ layers was investigated by using corroborative force−current measurements. Figure 2a presents temporal responses of force vs current obtained from 2D $SnSe_{2-x}$ layers grown on a PI substrate (inset image), measured at zero bias with a motorized force tester (Mark-10 ESM303). ObservatiOn of the bidirectional current generation and its subsequent increase upon a cycle of compressing/releasing forces indicates pressure-dependent piezoelectricity, which is mainly attributed to the SnSe phases with large piezoelectric coefficients and non-centrosymmetric structures.[4] Figure 2b shows a correlation of maximum piezoelectric current vs applied pressure obtained under compression (blue) and release (red) forces, yielding a highly linear relationship. In fact, multiple studies, including one on single-phased SnSe, have demonstrated intrinsic polarization-driven piezoelectricity, contextualizing the observed behavior.[32−35] The mechanical bendability of the $SnSe_{2-x}$/PI sample is demonstrated in Figure 2c, where r represents the radius of each curvature (red circle) and ε represents its corresponding bending strain. The ε values are calculated based on the diagram in Figure 2d using $\varepsilon = \frac{h}{2r}$,[35−37] where h and r represent the thickness of PI and the whole radius of the $SnSe_{2-x}$/PI sample under bending, respectively. For the calculation, it is reasonably assumed that the thickness of 2D $SnSe_{2-x}$ layers is negligible compared to those of h and r. Figure 2e illustrates a schematic of concave vs convex bending systematically applied (i.e., "ON") to the sample, which is to be employed for corroborative bending strain−piezo-current characteristics. The $SnSe_{2-x}$/PI sample is subjected to continuous current−voltage (I−V) sweeps under a sequences of concave vs convex bending with varying ε values, as presented in Figures 2f and 2g, respectively. Figure 2f presents a steady increase in the current with increasing degrees of concave (compressive) bending, while Figure 2g shows a current decrease with increasing degrees of convex

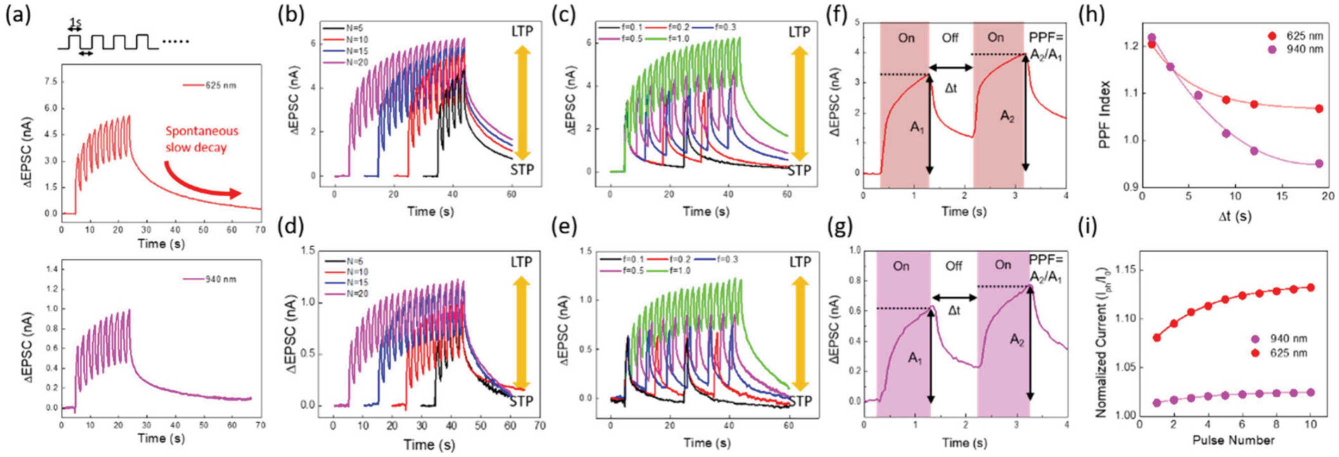

Figure 4. Illumination pulse-controlled optical introduction of broadband synaptic plasticity in $SnSe_{2-x}$/PI. (a) Synaptic plasticity characteristics introduced by 1 s interval pulses repeated for 10 times at wavelengths of 625 nm (top) and 940 nm (bottom). (b, c) 625 nm pulse-enabled STP/LTP characteristics manifested by ΔEPSC values with varying conditions of (b) pulse number and (c) frequency. (d, e) 940 nm pulse-enabled STP/LTP characteristics manifested by ΔEPSC values with varying conditions of (d) pulse number and (e) frequency. (f, g) PPF determination plots obtained at wavelengths of (f) 625 nm and (g) 940 nm. (h) PPF indexing modulated by EPSC variations under initial (A_1) and secondary (A_2) stimuli at wavelengths of 625 and 940 nm. (i) Wavelength-dependent normalization of photocurrents for each illumination pulse, extracted from (a).

(tensile) bending. The enlarged views of the red-boxed $I-V$ characteristics in Figures 2f and 2g are presented in Figures 2h and 2i, respectively. The results highlight a noticeable increase (Figure 2h) vs decrease (Figure 2i) of the current under concave vs convex bending, respectively. This observation of the directionality-dependent anisotropic current generation is highly consistent with the bidirectional piezoelectricity observed in Figure 2a. Furthermore, it reflects the electrical polarization-associated flexoelectric nature of 2D $SnSe_{2-x}$ layers driven by an uneven distribution of strain gradients within them, similarly observed in a wide range of polarized materials.[38−40] The observed anisotropic piezoelectricity is further studied with time-variant measurements of bending cycles vs piezo currents. Figures 2j and 2k demonstrate temporal responses of the piezo-current generation upon periodically applied concave and convex bending, respectively. Consistent with Figures 2h and 2i, the sample exhibits anisotropic piezoresponses manifested by opposite current directionalities. Specifically, for concave bending, the current increases during the ON state (bending) and decreases during the OFF state (return to the unbent state), whereas for convex bending, the current decreases during the ON state and increases during the OFF state. The experiments were performed involving 20 s of bending cycles with 10 s of rest and 20 s of return intervals, measured at a fixed strain rate of 1 mm/s and 3 V bias.

Toward the projected integration of the anisotropic piezoelectricity of 2D $SnSe_{2-x}$ layers into optoelectronic applications, their intrinsic carrier transport properties were characterized by field-effect transistor (FET) responses. Figure 3a presents an FET output curve of drain−source current (I_{ds}) vs drain−source voltage (V_{ds}) characteristics obtained from a back-gated FET employing 2D $SnSe_{2-x}$ layers directly grown on a SiO_2/Si wafer. A schematic illustration of the back-gated FET device is presented in Supporting Information, Figure S5. The FET (inset image) exhibits an increase in I_{ds} with increasing back-gate voltage values (V_g: legend), indicating n-type semiconducting characteristics of the 2D $SnSe_{2-x}$ layers-based channel. This n-type behavior is attributed to the $SnSe_2$ phase within the sample, as stoichiometric 2D $SnSe_2$ layers are known to be n-type semiconductors, according to previous FET studies.[41−43] Figure 3b displays the corresponding $I_{ds}-V_g$ curve, further confirming the n-type gate response, where the linearity of the curve[44] yields an electron mobility of ∼2 cm^2 $V^{-1}s^{-1}$. Figure 3c presents an $I-V$ plot obtained from a $SnSe_{2-x}$/PI sample patterned with gold (Au) interdigitated electrodes (IDEs), confirming its highly Ohmic transport. In Figure 3d through Figure 3g, the photoresponsiveness of other $SnSe_{2-x}$/PI samples associated with their semiconducting nature was systematically studied under varying illumination conditions, as demonstrated with individual SnSe[45,46] and $SnSe_2$.[47,48] Figure 3d shows temporal responses of photocurrent generations under periodic illuminations with an interval of 30 s and varying intensities, measured at a wavelength of 625 nm. Figure 3e presents the corresponding correlation of light intensity vs maximum photocurrent, revealing a high linearity. Similar photoresponsiveness characteristics are also observed at a different wavelength of 940 nm, as manifested by the temporal current responses (Figure 3f) and the linearity of intensity−photocurrent (Figure 3g), confirming the broadband nature of 2D $SnSe_{2-x}$ layers across visible to NIR spectral ranges. The wavelength-dependent spatial responsivity values, determined from the linear slopes in Figures 3e and 3g, are 6.58 nA m^2/W at 625 nm and 0.43 nA m^2/W at 940 nm, respectively.

Having confirmed the intrinsic photoresponsiveness of 2D $SnSe_{2-x}$ layers, we set out to explore their optically modulated synaptic plasticity toward artificial synapses and neuromorphic applications. The optical synaptic characteristics of $SnSe_{2-x}$/PI samples were characterized under repetitive and instantaneous application/cessation of optical pulse stimuli. The artificial synapse model by Atkinson and Shiffrin[49] simulates the human brain's learning/forgetting mechanisms as an interplay of optical stimuli and consequential electrical responses that are registered in sensory memories. Repetitively applied external stimuli, such as optical pulses, generate electrical signals in the surrounding environment of organs, representing short-term memory (STM) that lasts for a few seconds to minutes,

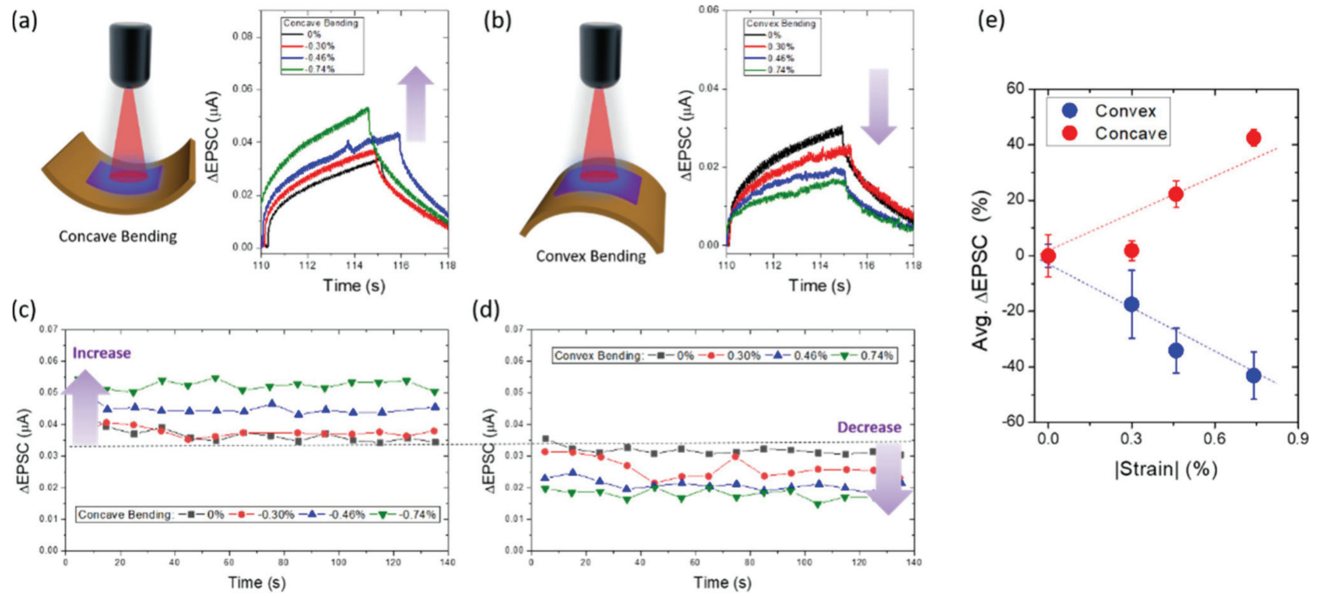

Figure 5. Modulation of synaptic photoresponsiveness by piezostrain coupling using a 405 nm laser source. (a, b) Enhancement and suppression of ΔEPSC by (a) concave (compressive) and (b) convex (tensile) bending, respectively. (c, d) Time-dependent systematic modulation of ΔEPSC revealing (c) concave strain-driven enhancement and (d) convex strain-driven suppression. (e) Average values of maximum ΔEPSC enhanced vs suppressed by convex vs concave bending with varying strain values.

mimicking the learning process. This short-term retention of stored information can be spontaneously converted to long-term memory (LTM) with much longer durations, simulating the forgetting process.[50] Accordingly, realizing the optically modulated STM-to-LTM transition is essential for demonstrating the entire learning/forgetting process of artificial synapses, which should accompany repetitive and instantaneous applications of stimuli for very short terms (typically, < a few seconds). Figure 4a demonstrates the short-term plasticity (STP) and long-term plasticity (LTP) characteristics of a representative $SnSe_{2-x}$/PI device under illuminations at wavelengths of 625 nm (top) and 940 nm (bottom) (i.e., visible to near-IR range). The STP characteristics were introduced by optical pulses with small intervals of 1 s, much smaller than the 30 s adopted for the photoresponsiveness measurements in Figure 3d and 3f. The optically potentiated device exhibits the LTP characteristics manifested by a slow and spontaneous decay of the generated photocurrent (i.e., change in excitatory postsynaptic current (ΔEPSC)), which is realized once the illuminations are terminated. Figures 4b and 4c present illumination-condition-dependent STP/LTP characteristics at a wavelength of 625 nm, manifested by a variation of pulse number, *N*, and pulse frequency, *f*, respectively. Noticeable transitions of STP to LTP are observed irrespective of the pulse condition variations, indicating the optically modulated synaptic plasticity of 2D $SnSe_{2-x}$ layers. Similar transition characteristics are also observed under 940 nm illumination, as demonstrated with a variation of *N* (Figure 4d) and *f* (Figure 4e). The STM and LTM-associated synaptic characteristics are attributed to the presence of high-density localized charge-trapping sites introduced by Se vacancies and grain boundaries inherent to the co-phased $SnSe_{2-x}$ films. This defect-mediated alteration of charge carrier dynamics, i.e., persistent photoconductivity (PPC)-driven memory effect, is generally responsible for optically induced synaptic phenomena involving the capture and release of electron−hole pairs over varying time scales.[50,51] In this regard, the PPC memory retention characteristics can be improved by optimizing the defect densities in $SnSe_{2-x}$ films through CVD condition adjustments, enabling a balance between their STM and LTM dynamics and thereby enhancing their suitability for neuromorphic applications. Paired-pulse facilitation (PPF) is another crucial parameter used to identify the proficiency of artificial synapses, which is defined as the EPSC ratio corresponding to two consecutive optical stimuli.[18] Figures 4f and 4g illustrate the PPF indexing achieved at 625 and 940 nm illuminations, respectively, under optical pulses with on/off intervals of 1 s for each wavelength. Figure 4h depicts comprehensive PPF indexing curves obtained with EPSC variations under a series of A_1 and A_2 stimuli. The fitting curves are derived from eq 1:

$$\text{PPF index} = c_1\cdot\exp\left(\frac{\Delta t}{\tau_1}\right) + c_2\cdot\exp\left(\frac{\Delta t}{\tau_2}\right) + 1 \quad (1)$$

where the relaxation times τ_1 (or τ_2) correspond to the fast (or slow) phase of the PPF index, respectively. The amplitude of the fast (or slow) phase is implied by c_1 (or c_2), corresponding to the initial facilitation values. Generally, τ_2 has a value distinctively larger than that of τ_1, indicating successive synaptic operations.[51] An observation of the gradual decrease in PPF indexing values as a function of interval period, Δ*t*, confirms that the 2D $SnSe_{2-x}$ layers possess the desired synaptic characteristics. Furthermore, Figure 4i displays a plot of the normalized photocurrent ratio with respect to the dark current as a function of *N*, extracted from Figure 4a. The steady decrease in the relative photocurrent for adjacent *N* values indicates a gradual decrease in ΔEPSC ratios, consistent with the PPF indexing results. Overall, through the comprehensive characterizations in Figure 4, the $SnSe_{2-x}$/PI device is confirmed to effectively function as an artificial synapse, simulating essential features of the human brain's functionalities under broadband stimuli.

Lastly, we demonstrate the enhancement of the optical synaptic plasticity of $SnSe_{2-x}$/PI devices by harnessing their piezoelectricity through a fine modulation of piezo-strains,[14,17,52−55] toward further strengthening their potential for flexible neuromorphic applications. Figure 5a demonstrates the piezo-driven enhancement of the synaptic response (i.e., ΔEPSC) of a device undergoing concave bending with systematically varying bending strains. The photocurrent is observed to steadily increase with increasing concave bending strain values, consistent with the predictions based on the observations without illuminations in Figure 2f and 2h. Conversely, when subjected to a convex bending, as demonstrated in Figure 5b, the identical device exhibits exactly opposite characteristics; that is, ΔEPSC decreases with more significant bending. The negativity (or positivity) of the values represent the concave (or convex) bending, respectively. Figures 5c and 5d demonstrate temporal responses of maximum ΔEPSC values obtained under concave and convex bending cycles, respectively, with various strain values. It is worth mentioning that the illumination distances during the cycles are maintained to be constant, thus ruling out any possibility of illumination intensity changes, which further confirms that the synaptic modulation was driven by the bidirectional piezoelectricity of the device. Figure 5e shows a correlation of average ΔEPSC obtained during the bending cycles with the absolute values of bending strains, revealing a significant piezo-photonic enhancement (or reduction) of up to ∼40% by a strain of <1%. It is worth emphasizing that this pronounced strain-driven modulation of photoresponsiveness and its synaptic applications were realized with “wafer-scale” CVD-grown 2D materials beyond mechanically exfoliated small 2D flakes. This accomplishment contributes to advancing strain-engineered dynamic mechano-optoelectronic functionalities in potentially “all-2D” systems of scaled-up dimensions accompanying matured fabrication technologies.

In summary, our investigations into the piezoelectricity-driven dynamic modulation of optical synapses inherent in wafer-scale 2D $SnSe_{2-x}$ layers reveal opportunities for flexible and adaptive neuromorphic devices. The co-phased $SnSe_{2-x}$ structure, synthesized via a controlled low-temperature CVD selenization reaction, uniquely integrates the complementary electronic and optical properties of SnSe and $SnSe_2$ phases, offering improved advantages for optoelectronic applications. Furthermore, this piezo-photonic coupling approach can be applied to a variety of semiconducting and polarized materials with intrinsic mechanical deformability, thus opening up a wide range of futuristic and transformative technologies. Accordingly, this study establishes a novel framework for mechano-optoelectronic flexible devices of practically relevant length scales.

■ ASSOCIATED CONTENT

Supporting Information

The Supporting Information is available free of charge at https://pubs.acs.org/doi/10.1021/acs.nanolett.4c04371.

> Experimental methods; AFM topography images and thickness measurements; XPS; HR-TEM; EDS line profile; and schematic illustration of back-gated FET (PDF)

■ AUTHOR INFORMATION

Corresponding Author

Yeonwoong Jung − *NanoScience Technology Center, University of Central Florida, Orlando, Florida 32826, United States; Department of Materials Science and Engineering and Department of Electrical and Computer Engineering, University of Central Florida, Orlando, Florida 32816, United States;* orcid.org/0000-0001-6042-5551; Email: yeonwoong.jung@ucf.edu

Authors

Changhyeon Yoo − *NanoScience Technology Center, University of Central Florida, Orlando, Florida 32826, United States*

Sang Sub Han − *NanoScience Technology Center, University of Central Florida, Orlando, Florida 32826, United States*

Chung Won Lee − *NanoScience Technology Center, University of Central Florida, Orlando, Florida 32826, United States*

Jebadiah Pond − *NanoScience Technology Center, University of Central Florida, Orlando, Florida 32826, United States; Department of Materials Science and Engineering, University of Central Florida, Orlando, Florida 32816, United States*

Yu-Jin Song − *Department of Materials Science and Engineering, Dong-A University, Busan 49315, Republic of Korea*

Jung Han Kim − *Department of Materials Science and Engineering, Dong-A University, Busan 49315, Republic of Korea;* orcid.org/0000-0002-6678-2282

Complete contact information is available at: https://pubs.acs.org/10.1021/acs.nanolett.4c04371

Author Contributions

C.Y. conceived the project idea and led the sample preparation and optical experiments under the guidance of Y.J. S.S.H. and J.P. assisted with sample preparation, testing, and characterization, also under Y.J.’s guidance. Y.-J.S. performed the structural characterization of the samples under the guidance of J.H.K. C.Y., S.S.H, C.W.L, and Y.J. wrote the manuscript with inputs from all authors.

Notes

The authors declare no competing financial interest.

■ ACKNOWLEDGMENTS

Y.J. acknowledges financial support from the U.S. National Science Foundation (CAREER: 2142310). S.S.H. acknowledges financial support from the Preeminent Postdoctoral Program (P3) at UCF. J.H.K. acknowledges support from the Ministry of Science and ICT (Project Number: 2024-22030006-00) and Commercialization Promotion Agency for R&D Outcomes (COMPA).

■ REFERENCES

(1) Martínez-Escobar, D.; Ramachandran, M.; Sánchez-Juárez, A.; Narro Rios, J. S. Optical and Electrical Properties of $SnSe_2$ and SnSe Thin Films Prepared by Spray Pyrolysis. *Thin Solid Films* **2013**, *535*, 390−393.

(2) Boscher, N. D.; Carmalt, C. J.; Palgrave, R. G.; Parkin, I. P. Atmospheric Pressure Chemical Vapour Deposition of SnSe and $SnSe_2$ Thin Films on Glass. *Thin Solid Films* **2008**, *516* (15), 4750−4757.

(3) Yang, F.; Wong, M.-C.; Mao, J.; Wu, Z.; Hao, J. Synthesis and Enhanced Piezoelectric Response of CVD-Grown SnSe Layered

Nanosheets for Flexible Nanogenerators. *Nano Research* **2023**, *16* (9), 11839−11845.

(4) Fei, R.; Li, W.; Li, J.; Yang, L. Giant Piezoelectricity of Monolayer Group IV Monochalcogenides: SnSe, SnS, GeSe, and GeS. *Appl. Phys. Lett.* **2015**, *107* (17), 173104.

(5) Gowthamaraju, S.; Deshpande, U. P.; Bhobe, P. A. Augmentation of the Thermoelectric Properties of Polycrystalline Tin Selenides via Formation of SnSe/$SnSe_2$ Composites. *J. Mater. Sci. Mater. Electron.* **2021**, *32* (9), 11781−11790.

(6) Madelung, O. *Data in Science and Technology: Semiconductors Other than Group IV Elements and III-V Compounds*; Springer-Verlag, 1992.

(7) Madelung, O. *Non-Tetrahedrally Bonded Elements and Binary Compounds I*; Springer-Verlag, 1998.

(8) Wang, B.; Zhong, S. P.; Zhang, Z. B.; Zheng, Z. Q.; Zhang, Y. P.; Zhang, H. Broadband Photodetectors Based on 2D Group IVA Metal Chalcogenides Semiconductors. *Appl. Mater. Today* **2019**, *15*, 115−138.

(9) Amalraj, L.; Jayachandran, M.; Sanjeeviraja, C. Preparation and Characterization of Tin Diselenide Thin Film by Spray Pyrolysis Technique. *Mater. Res. Bull.* **2004**, *39* (14), 2193−2201.

(10) Huang, Y.; Xu, K.; Wang, Z.; Shifa, T. A.; Wang, Q.; Wang, F.; Jiang, C.; He, J. Designing the Shape Evolution of $SnSe_2$ Nanosheets and Their Optoelectronic Properties. *Nanoscale* **2015**, *7* (41), 17375−17380.

(11) Liu, J.; Huang, Q.; Zhang, K.; Xu, Y.; Guo, M.; Qian, Y.; Huang, Z.; Lai, F.; Lin, L. High White Light Photosensitivity of SnSe Nanoplate-Graphene Nanocomposites. *Nanoscale Res. Lett.* **2017**, *12* (1), 259.

(12) Rani, S.; Kumar, M.; Singh, Y.; Tomar, M.; Sharma, A.; Gupta, V.; Singh, V. N. NO_2 Gas Sensor Based on SnSe/$SnSe_2$ pn Heterojunction. *J. Nanosci. Nanotechnol.* **2021**, *21* (9), 4779−4785.

(13) Jiang, H.-T.; Tian, H.; Sun, S.-T.; Cao, L.; Yin, C.-H.; Zhou, X.-L.; Lv, Y.-Y.; Zhou, J.; Yao, S.-H.; Chen, Y. B.; Chen, Y.-F. Enhanced Optical Responsivity in Photothermoelectric Effect of SnSe-$SnSe_2$ Composite at Near-Infrared Band. *Appl. Phys. Lett.* **2024**, *125* (3), 031103.

(14) Li, F.; Shen, T.; Wang, C.; Zhang, Y.; Qi, J.; Zhang, H. Recent Advances in Strain-Induced Piezoelectric and Piezoresistive Effect-Engineered 2D Semiconductors for Adaptive Electronics and Optoelectronics. *Nano-Micro Lett.* **2020**, *12* (1), 106.

(15) Wu, W.; Wang, Z. L. Piezotronics and Piezo-Phototronics for Adaptive Electronics and Optoelectronics. *Nat. Rev. Mater.* **2016**, *1* (7), 16031.

(16) Li, X.; Guo, J.; Wang, H.; Zheng, X.; Chen, Y.; Tang, J.; Lin, H.; He, L.; Li, C. Tri-MX: New Group-IV Monochalcogenide Monolayers with Excellent Piezoelectricity and Special Optical Properties. *Appl. Surf. Sci.* **2022**, *602*, 154391.

(17) Li, F.; Shen, T.; Xu, L.; Hu, C.; Qi, J. Strain Improving the Performance of a Flexible Monolayer MoS_2 Photodetector. *Adv. Electron. Mater.* **2019**, *5* (12), 1900803.

(18) Lee, C. W.; Yoo, C.; Han, S. S.; Song, Y.-J.; Kim, S. J.; Kim, J. H.; Jung, Y. Centimeter-Scale Tellurium Oxide Films for Artificial Optoelectronic Synapses with Broadband Responsiveness and Mechanical Flexibility. *ACS Nano* **2024**, *18* (28), 18635−18649.

(19) Han, S. S.; Shin, J.-C.; Ghanipour, A.; Lee, J.-H.; Lee, S.-G.; Kim, J. H.; Chung, H.-S.; Lee, G.-H.; Jung, Y. High Mobility Transistors and Flexible Optical Synapses Enabled by Wafer-Scale Chemical Transformation of Pt-Based 2D Layers. *ACS Appl. Mater. Interfaces* **2024**, *16* (28), 36599−36608.

(20) Yoo, C.; Ko, T.-J.; Kaium, M. G.; Martinez, R.; Islam, M. M.; Li, H.; Kim, J. H.; Cao, J.; Acharya, M.; Roy, T.; Jung, Y. A Minireview on 2D Materials-Enabled Optoelectronic Artificial Synaptic Devices. *APL Mater.* **2022**, *10* (7), 070702.

(21) Sierra-Castillo, A.; Haye, E.; Acosta, S.; Arenal, R.; Bittencourt, C.; Colomer, J.-F. Atmospheric Pressure Chemical Vapor Deposition Growth of Vertically Aligned SnS_2 and $SnSe_2$ Nanosheets. *RSC Adv.* **2021**, *11* (58), 36483−36493.

(22) Wu, J.; Hu, Z.; Jin, Z.; Lei, S.; Guo, H.; Chatterjee, K.; Zhang, J.; Yang, Y.; Li, B.; Liu, Y.; Lai, J.; Vajtai, R.; Yakobson, B.; Tang, M.; Lou, J.; Ajayan, P. M. Spiral Growth of $SnSe_2$ Crystals by Chemical Vapor Deposition. *Adv. Mater. Interfaces* **2016**, *3* (16), 1600383.

(23) Santhoshkumar, P.; Thirumalraj, B.; Sriram, B.; Karuppasamy, K.; Vikraman, D.; Kathalingam, A.; Choe, H.; Kim, H.-S. Mesoporous $SnSe_2$-Grafted N-Doped Carbon Composites with Integrated Flaky Structure for Electrochemical Sensing of Carbendazim. *Ceram. Int.* **2022**, *48* (11), 16023−16032.

(24) Xu, H.-H.; Zhou, N.-N.; Liang, X.-L.; Jiang, T.-T.; He, W.-T.; Song, J.-M. SnSe Nanoparticles with Ultra-Low Lattice Thermal Conductivity: Synthesis and Characterization. *J. Nanopart. Res.* **2022**, *24* (6), 109.

(25) Bernardes-Silva, A. C.; Mesquita, A. F.; de Moura Neto, E.; Porto, A. O.; de Lima, G. M.; Ardisson, J. D.; Lameiras, F. S. Tin Selenide Synthesized by a Chemical Route: The Effect of the Annealing Conditions in the Obtained Phase. *Solid State Commun.* **2005**, *135* (11), 677−682.

(26) Mandal, P.; Show, B.; Ahmed, S. T.; Banerjee, D.; Mondal, A. Visible-Light Active Electrochemically Deposited Tin Selenide Thin Films: Synthesis, Characterization and Photocatalytic Activity. *J. Mater. Sci. Mater. Electron.* **2020**, *31* (6), 4708−4718.

(27) Saha, S.; Banik, A.; Biswas, K. Few-Layer Nanosheets of n-Type $SnSe_2$. *Chem.—Eur. J.* **2016**, *22* (44), 15634−15638.

(28) Assili, K.; Gonzalez, O.; Alouani, K.; Vilanova, X. Structural, Morphological, Optical and Sensing Properties of SnSe and $SnSe_2$ Thin Films as a Gas Sensing Material. *Arab. J. Chem.* **2020**, *13* (1), 1229−1246.

(29) Okogbue, E.; Han, S. S.; Ko, T.-J.; Chung, H.-S.; Ma, J.; Shawkat, M. S.; Kim, J. H.; Kim, J. H.; Ji, E.; Oh, K. H.; Zhai, L.; Lee, G.-H.; Jung, Y. Multifunctional Two-Dimensional $PtSe_2$-Layer Kirigami Conductors with 2000% Stretchability and Metallic-to-Semiconducting Tunability. *Nano Lett.* **2019**, *19* (11), 7598−7607.

(30) Han, S. S.; Kim, J. H.; Noh, C.; Kim, J. H.; Ji, E.; Kwon, J.; Yu, S. M.; Ko, T.-J.; Okogbue, E.; Oh, K. H.; Chung, H.-S.; Jung, Y.; Lee, G.-H.; Jung, Y. Horizontal-to-Vertical Transition of 2D Layer Orientation in Low-Temperature Chemical Vapor Deposition-Grown $PtSe_2$ and Its Influences on Electrical Properties and Device Applications. *ACS Appl. Mater. Interfaces* **2019**, *11* (14), 13598−13607.

(31) Ko, T.-J.; Han, S. S.; Okogbue, E.; Shawkat, M. S.; Wang, M.; Ma, J.; Bae, T.-S.; Hafiz, S. B.; Ko, D.-K.; Chung, H.-S.; Oh, K. H.; Jung, Y. Wafer-Scale 2D $PtTe_2$ Layers-Enabled Kirigami Heaters with Superior Mechanical Stretchability and Electro-Thermal Responsiveness. *Appl. Mater. Today* **2020**, *20*, 100718.

(32) Alluri, N. R.; Raj, N. P. M. J.; Khandelwal, G.; Kim, S.-J. Shape-Dependent In-Plane Piezoelectric Response of SnSe Nanowall/Microspheres. *Nano Energy* **2021**, *88*, 106231.

(33) Yoo, C.; Adepu, V.; Han, S. S.; Kim, J. H.; Shin, J.-C.; Cao, J.; Park, J.; Al Mahfuz, M. M.; Tetard, L.; Lee, G.-H.; Ko, D.-K.; Sahatiya, P.; Jung, Y. Low-Temperature Centimeter-Scale Growth of Layered 2D SnS for Piezoelectric Kirigami Devices. *ACS Nano* **2023**, *17* (20), 20680−20688.

(34) Wang, Z.; Wang, L.; Ren, W.; Li, C.; Quan, Y.; Zheng, K.; Zhuang, J. The Vertically Heteroepitaxial Structure for Lead-Free Piezoelectric $K_{0.5}Na_{0.5}NbO_3$ Films. *Crystals* **2023**, *13* (3), 525.

(35) Zheng, W.; Tang, Y.; Liu, Z.; Xing, G.; Zhao, K. Enhanced Charge Carrier Separation by Bi-Piezoelectric Effects Based on Pine Needle-Like $BaTiO_3$/ZnO Continuous Nanofibers. *J. Mater. Chem. A* **2022**, *10* (25), 13544−13555.

(36) Dai, M.; Chen, H.; Wang, F.; Hu, Y.; Wei, S.; Zhang, J.; Wang, Z.; Zhai, T.; Hu, P. Robust Piezo-Phototronic Effect in Multilayer γ-InSe for High-Performance Self-Powered Flexible Photodetectors. *ACS Nano* **2019**, *13* (6), 7291−7299.

(37) Wu, W.; Wang, L.; Yu, R.; Liu, Y.; Wei, S.-H.; Hone, J.; Wang, Z. L. Piezophototronic Effect in Single-Atomic-Layer MoS_2 for Strain-Gated Flexible Optoelectronics. *Adv. Mater.* **2016**, *28* (38), 8463−8468.

(38) Ahmadpoor, F.; Sharma, P. Flexoelectricity in Two-Dimensional Crystalline and Biological Membranes. *Nanoscale* **2015**, *7* (40), 16555−16570.

(39) Springolo, M.; Royo, M.; Stengel, M. Direct and Converse Flexoelectricity in Two-Dimensional Materials. *Phys. Rev. Lett.* **2021**, *127* (21), 216801.

(40) Zhuang, X.; He, B.; Javvaji, B.; Park, H. S. Intrinsic Bending Flexoelectric Constants in Two-Dimensional Materials. *Phys. Rev. B* **2019**, *99* (5), 054105.

(41) Xu, H.; Xing, J.; Huang, Y.; Ge, C.; Lu, J.; Han, X.; Du, J.; Hao, H.; Dong, J.; Liu, H. $SnSe_2$ Field-Effect Transistor with High On/Off Ratio and Polarity-Switchable Photoconductivity. *Nanoscale Res. Lett.* **2019**, *14* (1), 17.

(42) Su, Y.; Ebrish, M. A.; Olson, E. J.; Koester, S. J. $SnSe_2$ Field-Effect Transistors with High Drive Current. *Appl. Phys. Lett.* **2013**, *103* (26), 263104.

(43) Guo, C.; Tian, Z.; Xiao, Y.; Mi, Q.; Xue, J. Field-Effect Transistors of High-Mobility Few-Layer $SnSe_2$. *Appl. Phys. Lett.* **2016**, *109* DOI: 10.1063/1.4967744.

(44) Streetman, B. G.; Banerjee, S. *Solid State Electronic Devices*; Prentice Hall, NJ, 2000.

(45) Xu, H.; Hao, L.; Liu, H.; Dong, S.; Wu, Y.; Liu, Y.; Cao, B.; Wang, Z.; Ling, C.; Li, S.; Xu, Z.; Xue, Q.; Yan, K. Flexible SnSe Photodetectors with Ultrabroad Spectral Response up to 10.6 μm Enabled by Photobolometric Effect. *ACS Appl. Mater. Interfaces* **2020**, *12* (31), 35250−35258.

(46) Wang, H.; Zhang, S.; Zhang, T.; Liu, J.; Zhang, Z.; Yuan, G.; Liang, Y.; Tan, J.; Ren, Y.; Lei, W. SnSe Nanoplates for Photodetectors with a High Signal/Noise Ratio. *ACS Appl. Nano Mater.* **2021**, *4* (12), 13071−13078.

(47) Gupta, S. U.; Dalvaniya, A. G.; Limberkar, C.; Patel, K. D.; Solanki, G. K.; Pathak, V. M.; Pataniya, P. M.; Sumesh, C. K.; Som, N. N.; Jha, P. K.; Patel, V. Annealing Induced Phase Transformation from Amorphous to Polycrystalline $SnSe_2$ Thin Film Photodetector with Enhanced Light-Matter Interaction. *J. Non-Cryst. Solids* **2022**, *578*, 121353.

(48) Gupta, S. U.; Dalvaniya, A. G.; Patel, N. F.; Bhakhar, S. A.; Nair, S.; Joy, J.; Patel, K. D.; Solanki, G. K.; Pathak, V. M.; Som, N. N.; Jha, P. K.; Panda, D. K. Optical Switching Device Based on a Crystalline $SnSe_2$ Photodetector in Diverse Conditions. *ACS Appl. Electron. Mater.* **2021**, *3* (11), 4859−4869.

(49) Atkinson, R. C.; Shiffrin, R. M. Human Memory: A Proposed System and its Control Processes. In *Psychology of Learning and Motivation*; Spence, K. W.; Spence, J. T., Eds.; Academic Press, 1968; Vol. *2*; pp 89−195.

(50) Chang, T.; Jo, S.-H.; Lu, W. Short-Term Memory to Long-Term Memory Transition in a Nanoscale Memristor. *ACS Nano* **2011**, *5* (9), 7669−7676.

(51) Jeong, B. H.; Park, J.; Kim, D.; Lee, J.; Jung, I. H.; Park, H. J. Visible Light-Sensitive Artificial Photonic Synapse. *Adv. Optical Mater.* **2024**, *12* (4), 2301652.

(52) Qu, L.-H.; Yu, J.; Mu, Y.-L.; Fu, X.-L.; Zhong, C.-G.; Min, Y.; Zhou, P.-X.; Zhang, J.-M.; Zou, Y.-Q.; Lu, T.-S. Strain Tunable Structural, Mechanical and Electronic Properties of Monolayer Tin Dioxides and Dichalcogenides SnX_2 (XO, S, Se, Te). *Mater. Res. Bull.* **2019**, *119*, 110533.

(53) Pandey, A.; Sharma, S.; Gangwar, A. K.; Kaur, M.; Singh, P.; Husale, S. Strain-Induced Photocurrent Enhancement in Thin Films of Topological Insulators (Bi_2Te_3). *J. Mater. Chem. C* **2023**, *11* (40), 13838−13847.

(54) Li, F.; Lu, Z.; Lan, Y.-W.; Jiao, L.; Xu, M.; Zhu, X.; Zhang, X.; Wu, H.; Qi, J. Force and Light Tuning Vertical Tunneling Current in the Atomic Layered MoS_2. *Nanotechnology* **2018**, *29* (27), 275202.

(55) Ding, R.; Lyu, Y.; Wu, Z.; Guo, F.; Io, W. F.; Pang, S.-Y.; Zhao, Y.; Mao, J.; Wong, M.-C.; Hao, J. Effective Piezo-Phototronic Enhancement of Flexible Photodetectors Based on 2D Hybrid Perovskite Ferroelectric Single-Crystalline Thin-Films. *Adv. Mater.* **2021**, *33* (32), 2101263.